

Numerical Simulation of Control Surface Deflections over a Generic UCAV Configuration at Off-design Flow Conditions

D.J. Kennett*, G. Hoholis† and K.J. Badcock‡

School of Engineering, University of Liverpool

Liverpool, L69 3BX, United Kingdom

The ability of computational fluid dynamics to predict the steady and unsteady fluid flow over a generic UCAV configuration, with and without control surface deflections, at off design conditions is investigated. The complex, non-linear flow, various combinations of control surface deflection and the presence of multiple interacting vortices on the flow histories provides a challenging test for current capability. A range of static and dynamic test cases have been computed, for both low and high speed flows, for comparison with experimental data, obtained as part of the NATO STO AVT-201 Task Group. The simulations are performed using a multiblock code to solve the Reynolds-Averaged Navier-Stokes equations; and the control surfaces are modelled with a deformed mesh and blended gaps that simplify the geometry. These tests will provide an assessment of the ability of computational fluid dynamics to evaluate such flows, and will allow for deficiencies in the state of the art to be identified.

Nomenclature

α	=	AoA, Angle of attack [°]	A	=	Amplitude [°]
β	=	AoS, Angle of sideslip [°]	MRP	=	Moment Reference Point
η	=	Flap deflection angle [°]	s	=	Half span [m]
Θ	=	Pitch angle [°]	c_{ref}	=	Reference length [m]
Ψ	=	Yaw angle [°]	c_r	=	Length of root chord [m]
V	=	On flow velocity [m/s]	C_p	=	Pressure coefficient
f	=	Frequency [Hz]	C_L	=	Lift coefficient [-]
t	=	Time [t]	C_D	=	Drag coefficient [-]
y	=	Span wise coordinate [m]	C_Y	=	Side force coefficient (AE) [-]
x	=	Chord wise coordinate [m]	C_{my}	=	Pitch moment coefficient (body) [-]
z	=	Vertical coordinate [m]	C_{mx}	=	Roll moment coefficient (body) [-]
k	=	Reduced frequency $\pi \cdot f \cdot c_{ref} / V$	C_{mz}	=	Yaw moment coefficient (body) [-]

I. Introduction

In recent years there has been interest in understanding the flow around delta wing-body Unmanned Combat Aircraft Vehicles (UCAV) and in determining the ability of computational fluid dynamics (CFD) to capture the flow physics associated with them. The SACCON¹ is a generic UCAV model, and was designed with the intention of validating CFD methods for complicated flow regimes with experimental measurements. It features a lambda planform, with a leading edge sweep angle of 53° and a wing washout of 5°, as shown in Fig. 1(a). The leading edge of the SACCON is sharp near the apex, and becomes rounded along the

*Research Associate, School of Engineering, corresponding author, Tel: +44151-794-8035, Email: D.Kennett@liv.ac.uk

†PhD Candidate, CFD Laboratory, School of Engineering, ghoholis@liverpool.ac.uk.

‡Professor, School of Engineering, K.J.Badcock@liverpool.ac.uk, Senior Member AIAA.

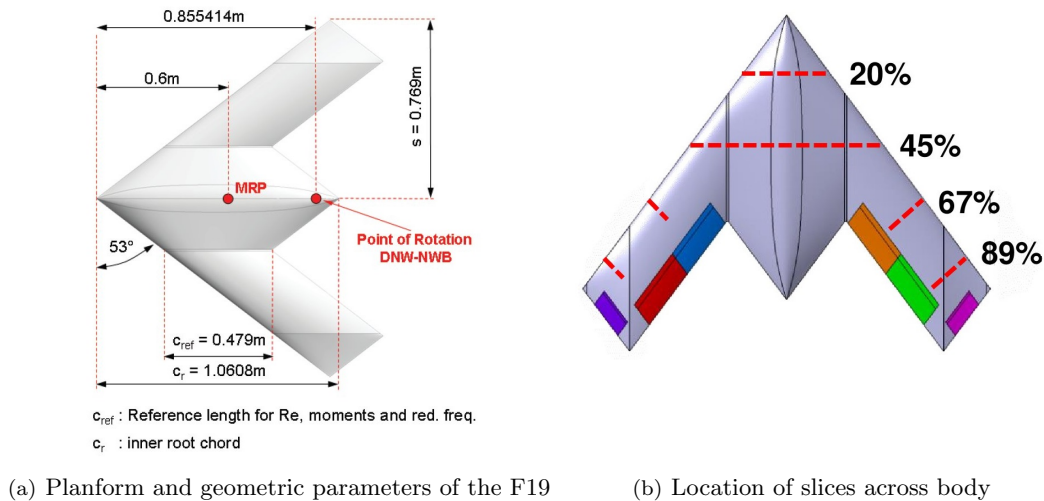


Figure 1. SACCON geometry.

mid-section, before becoming sharp again towards the tip-section. It was designed to generate vortical flows, as opposed to optimising for certain flight regimes, as is done in conventional aircraft wing design.

The NATO RTO AVT-161 Task Group² was established to determine the ability of computational methods to accurately predict both static and dynamic stability characteristics of air and sea vehicles. As part of this group, the flow physics of the SACCON was studied, and the predictions of CFD determined. The major features of the flow regime can be described using Fig. 2 (taken from Ref.³), which shows the experimental results for the pitching moment coefficient by variation of the angle of attack, and describes the changes in the flow topology at various points.

At low α , the sharp leading edge near the apex causes an apex vortex. Due to the rapidly increasing leading edge radius in the span wise direction, the corresponding flow separation is confined to a small region at the front part only; while further downstream the flow is attached along the whole leading edge. This also applies for the tip region of the wing, where the leading edge radius is very small, but the local α is reduced due to the geometrical twist. With increasing angle of attack, this flow pattern remains unchanged; and, as Fig. 2 shows, the apex vortex strength causes the nose up pitching moment to increase.

Starting at $\alpha = 11^\circ$, in the outer region of the wing a tip vortex is formed: its onset point moves upstream with increasing angle of attack. The suction underneath the tip vortex produces local lift behind the MRP, and this leads to an additional nose down pitching moment contribution, which is marked in Fig. 2 in red. This continues until about $\alpha = 14^\circ$, when the formation of the tip vortex is complete. For further increasing angle of attack the tip vortex onset point does not continue to move upstream since the leading edge radius increases in the upstream direction, and flow separation is therefore suppressed. The position of the tip vortex is frozen for the range $14^\circ \leq \alpha \leq 16^\circ$, in which the pitching moment coefficient increases due to the suction caused by the apex vortex, while the nose down contribution to the pitching moment remains virtually constant.

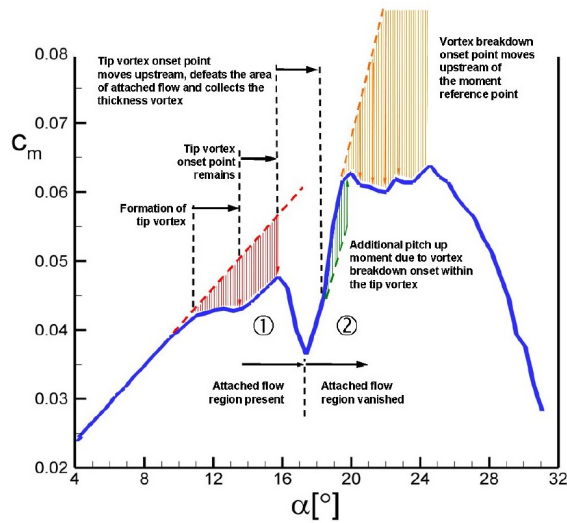


Figure 2. Pitching moment coefficient as function of α with an interpretation how the vortex flow topology is affecting the aerodynamic behavior. Taken from Ref.³

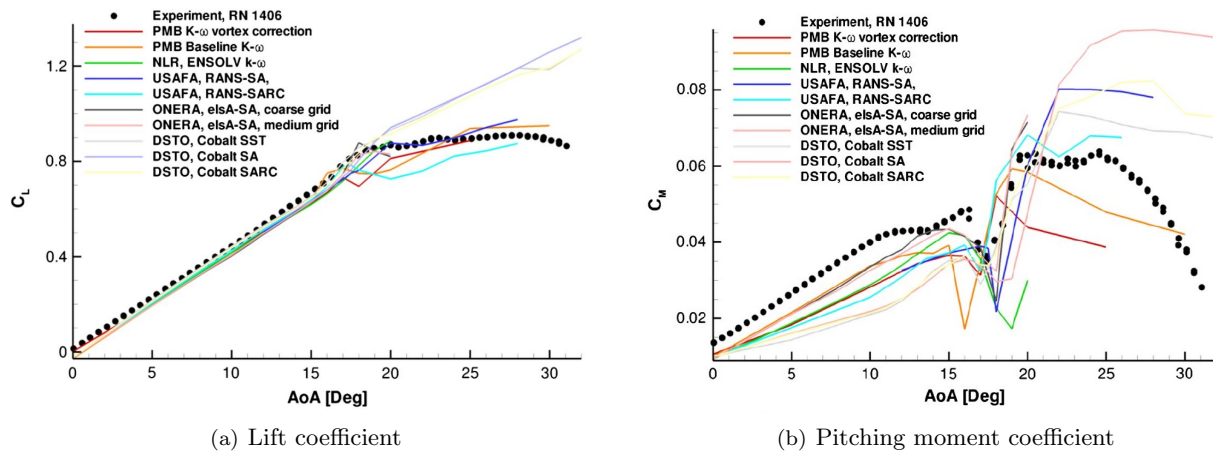


Figure 3. SACCON code-to-code comparison of lift and pitching moment coefficients without sting, $M=0.17$, $Re=1.93 \times 10^6$. Taken from Ref.⁴

As the angle of attack increases to $\alpha > 16^\circ$ the tip vortex onset point moves upstream. The strength of the tip vortex is enlarged and the additional nose down pitching moment contribution increases as well, causing a dip in the pitching moment coefficient, Fig. 2. At the centre of the dip in the pitching moment slope, the region of attached flow at the leading edge disappears. The upstream movement of the tip vortex is now no longer hindered, and this vortex develops into a large outer vortex. Since its suction also now affects the wing portion in front of the MRP, the tendency of the pitching moment characteristic is reversed. Beyond the dip at higher angles of attack, large nose up pitching moment contributions are created by the increasing suction in the front part of the configuration; and above this angle vortex break down occurs.

A comparison of the results from CFD codes used by members of the group to predict the lift and pitching moment coefficients are given in Fig 3 (taken from Ref.⁴); these results are for the case when the experimental sting is not modelled, as that is done in this work. The lift coefficient predictions, in Fig. 3(a), show that for angles of attack up to approximately 15° , the predictions were all very similar: yet all predict values slightly lower than the experimental data. When the sting is included in the grid modelling⁴ the comparisons with data up to a 15° angle of attack were in much better agreement with the experiment. Beyond the 15° angle of attack there is a fairly wide range of prediction in the non-linear region. For the pitching moment coefficient, shown in Fig. 3(b), at angles up to 15° none of the predictions match the experimental data trend, either in magnitude or slope; and although all codes predicted a dip, many of them predicted the behavior at an angle of attack that differed by two to three degrees.

The AVT-201 Task Group⁵ is an extension of the AVT-161 Task Group, and builds on the work to include control surface deflections for the SACCON at both high and low speed Mach numbers. The flow regime of interest is limited to the lower angle of attack, before the pitching moment dip. For the low speed calculations the angles of attack are $\alpha = 10^\circ$ and $\alpha = 15^\circ$; as a result, they simulate the cases before and after the tip vortex of the SACCON is formed. In this way, the CFD can predict the flow when it is relatively benign, and when the non-linearities begin. Forced motion oscillations are also included, in which the presence of multiple interacting vortices raises the possibility of significant history effects on the forces and moments. The low speed experimental data was obtained from the DNW-NWB wind-tunnel in Braunschweig, Germany;^{6,7} and the high speed experimental data was obtained from the BAE Systems wind-tunnel in Warton, England.⁸

This paper attempts to establish the state-of-the-art by solving the Reynolds-Averaged Navier-Stokes (RANS) equations in this angle of attack range. The control surface deflections are modelled on structured, multiblock grids by using a mesh deformation, with a blending region between the flap and body. The low speed and high speed steady state test cases included in this work are summarised in Table 1 (control surfaces are labelled left-outboard (LOB), left-inboard (LIB), right-outboard (ROB) and right-inboard (RIB)). Low speed calculations are performed in Section III, at $M=0.146$, $Re=1.57 \times 10^6$; and the high speed cases are performed in Section IV, at $M=0.7$, $Re=18.81 \times 10^6$. High speed calculations are performed at $\alpha = 5^\circ$ and $\alpha = 10^\circ$, as the higher Mach and Reynolds numbers effectively lower the angle of attack range. The unsteady, forced motion simulations are summarised in Table 2, and are performed in Section V. They are forced pitch and yaw motions, and take place at the same nominal pitch angles used in the steady calculations. The AVT-

Experiment	M	Re [$\cdot 10^6$]	LOB	LIB	ROB	RIB	α [$^\circ$]	β [$^\circ$]
RN1007	0.146	1.57	0	0	0	0	10	0, 5, 10
RN1008	0.146	1.57	0	0	0	0	15	0, 5, 10
RN1092	0.146	1.57	0	-20	+20	0	10, 15	0
RN1114	0.146	1.57	-20	0	0	+20	10, 15	0
RN1103	0.146	1.57	-20	-20	+20	+20	10, 15	0
40046	0.7	18.81	0	0	0	0	5, 10	0
40078	0.7	18.81	+10	0	0	0	5, 10	0
40071	0.7	18.81	-10	0	0	0	5, 10	0
40099	0.7	18.81	0	+10	0	0	5, 10	0
40104	0.7	18.81	0	-10	0	0	5, 10	0

Table 1. Summary of steady state cases performed from the AVT-201 common test matrix.

Experiment	Mode	Θ_0 [$^\circ$]	f(Hz)	A [$^\circ$]	Steps per cycle
2342-50	pitch	10	1	4.7	128, 256, 512
2360-68	pitch	15	1	4.7	128, 256, 512, 1024
2270-78	yaw	10	1	5.0	128, 256, 512
2288-96	yaw	15	1	5.0	128, 256, 512, 1024

Table 2. Summary of unsteady cases performed at $M=0.146$, $Re=1.57 \times 10^6$ (no control surface deflections).

201 common test matrix contains forced pitch and yaw motions at both 1Hz and 2Hz frequencies; however, the experimental data and previous CFD tests⁹ show more non-linearity for the low frequency oscillation cases ($f=1\text{Hz}$), which is presumed to be due to the flow dynamics having sufficient time to transition between states at the lower frequencies. At the higher oscillation frequencies ($f=2\text{Hz}$) the flow does not have time to transition, resulting in a more linear behavior. As a result, all of the test cases in this paper are at the lower oscillation frequency.

II. Solver details and grid generation

A. Solver details

The flow solver used for these calculations is a research code developed at the University of Liverpool called parallel multiblock (PMB).¹⁰ PMB uses a cell-centred method on block-structured meshes; and solves the Reynolds-Averaged Navier-Stokes (RANS) equations with Osher's Riemann solver, a monotone upwind scheme for convection laws variable extrapolation and a Van Albada limiter. A slightly modified $k - \omega$ turbulence model is used, which was introduced by Brandsma et al.,¹¹ to limit the amount of turbulent kinetic energy produced within the vortex core. The solver does not use wall functions, and the flow is assumed to be fully turbulent. The mean and turbulent equations are solved decoupled in an implicit manner, with approximate Jacobian matrices based on the first order sparsity pattern, and a Krylov subspace iterative solver. At the far-field the boundary conditions are simply set to freestream values; this treatment assumes that the boundary is located far enough to allow the flow to return to freestream conditions. The grids used in this work have a far-field that is 20 times the reference chord length away from the geometry, which is a sufficient distance for this to occur. Ghost cells are used for the solid wall boundary conditions - there are two adjacent to the wall. The steady state solutions were judged to be converged when the residual had converged to six orders of magnitude, based on the residual after the first pseudo-time step. Each of the computations were performed in parallel on the UK national supercomputing service.

Model	Grid spacing [$.c_{ref}$]	Number of points [$.10^6$]	Number of cells [$.10^6$]
F19	1×10^{-5}	15.225	14.030
F17-E	1×10^{-6}	17.742	16.440

Table 3. Summary of grids used.

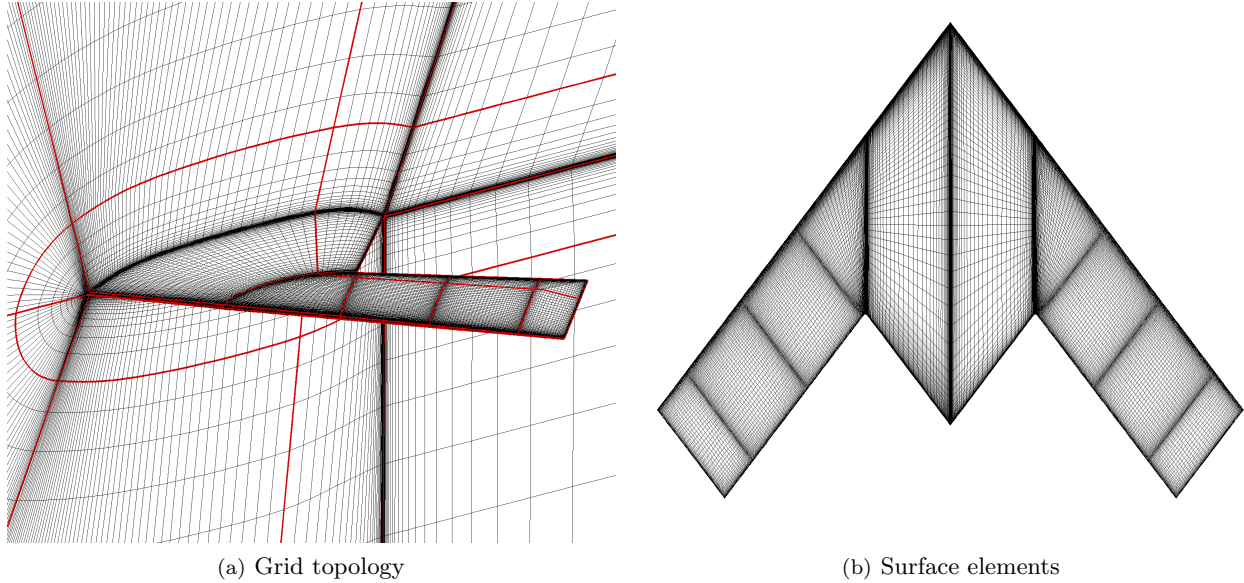


Figure 4. Views of the grid used for the calculations in this report.

For time-accurate simulations, a temporal integration is performed using an implicit dual time-stepping method.¹² In PMB the time step is non-dimensionalised using the length scale of the grid and the freestream velocity as follows,

$$\hat{t} = t \frac{V}{c_{ref}} \quad (1)$$

One non-dimensional time step, \hat{t} , is essentially how long it takes for a particle to travel the unit length of the grid in real-time. The grids in this work were made to match the model size, so a unit grid size is $1m$ of the model. The non-dimensional frequency k , is obtained from the following equation,

$$k = \frac{\pi c_{ref} f}{V} \quad (2)$$

The solution was judged to be converged, at each real-time step, when the residual had converged to three orders of magnitude, based on the residual after the first pseudo-time step. A maximum of 100 pseudo-time steps was allowed for this to occur. The numerical results contain the time histories of the oscillatory motions when convergence is reached; and, for these simulations, two cycles was enough for the transients to damp out and the solution converge.

B. Grids with no control surface deflections

There are two different sized models used for the flow at various speeds: the low speed experiments were performed on the F19 model, and the high speed experiments were performed on the F17-E model. The reference lengths and geometric parameters of the F19 can be seen in Fig. 1(a). The two models, with no control surface deflections, are virtually identical, except the F17-E is scaled to a ratio of 1:2.563 with the F19, so is approximately 40% of the size; this gives the F17-E model a span of $0.6m$ and overall length of $0.489m$.

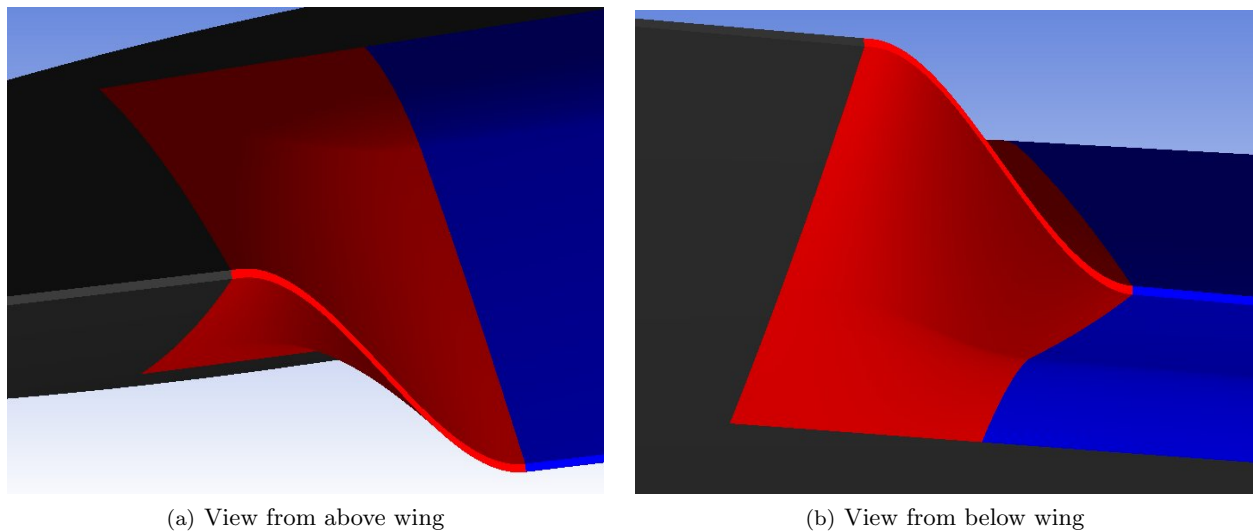


Figure 5. Screenshot of the region between the wing(grey) and flap(blue) used as a blending region(red) for the left inboard control surface deflection of $+20^\circ$.

The grids that were generated in this work all effectively come from one parent grid from which the others were made. The parent grid is for the F19 with no control surface deflections, and was generated using the grid generation software ANSYS ICEM. The geometry is the full CAD model of the SACCON; the major differences to the experimental setup are that the sting and walls of the wind-tunnel are not modelled. Work has previously been done using the SACCON geometry at the University of Liverpool^{13,14} as part of the AVT-161 Task Group. The best grid characteristics for this model using the PMB solver were determined; and, although a new set of grids was generated for use in this work, the lessons learnt were applied for the new grids that have been created. Based on these lessons, the first cell spacing normal to the solid wall is around $1 \times 10^{-5} c_{ref}$, which was sufficient to ensure that the boundary layer was well resolved for Reynolds numbers of the order of 1–2 million. The medium size grid was roughly 15 million points and 14 million cells, and this size is retained for this work; these points are spread across 260 blocks in total. The grid topologies are also very similar, with a C-blocking around the leading edge, an O-grid at the blunt tip and a H-grid around the trailing edge. The major difference is in the block construction near the wing surfaces, which are needed to create the family of grids with control surface deflections. The basic block topology of the grid can be seen in Fig. 4(a), and the discretisation of the upper surface can be seen in Fig. 4(b).

This grid was first validated, and the steady state results are presented in Section III.A. Unsteady, forced oscillation cases are simulated with this grid in Section V. The subsequent generation of the grids with control surface deflections is described in Section II.C.

The high speed cases are performed on the same grid, except the first cell spacing normal to the solid wall is around $1 \times 10^{-6} c_{ref}$, which is necessary to resolve the higher Reynolds number flow over the surface. This means that the grid has increased in size, and contains approximately 17 million points and 16 million cells. The properties of the grids used in this work are summarised in Table 3; the grids with control surface deflections are exactly the same size as the grid of their respective model with no deflections.

C. Grids with control surface deflections

The control surfaces are located at the trailing edge of the wings. Each model has two control surfaces on both the left and right wings; these are labelled left-outboard (LOB), left-inboard (LIB), right-outboard (ROB) and right-inboard (RIB). For the F19 the hinge line is at 75% of the reference chord; while for the F17-E the hinge line is located at 80%, so is not as large. In this work the control surfaces are deflected by $\pm 20^\circ$ for the F19 and $\pm 10^\circ$ for the F17-E.

The presence of the control surfaces introduces discontinuities into the surface, which must be modelled. Work has previously been done by Rampurawala¹⁵ on the treatment of control surfaces for full aircraft for use with structured multiblock solvers. This investigated two of the options available, which can be used with PMB in its current state: firstly, leaving the flap geometry as it is, and blocking the gap between the

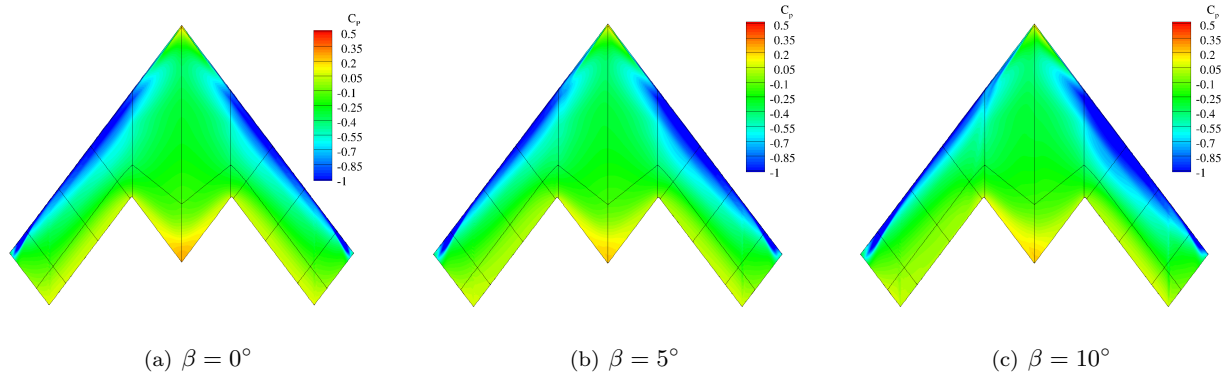


Figure 6. Run 1007 ($M=0.146$, $\alpha=10^\circ$, $Re=1.5709 \times 10^6$) surface contours.

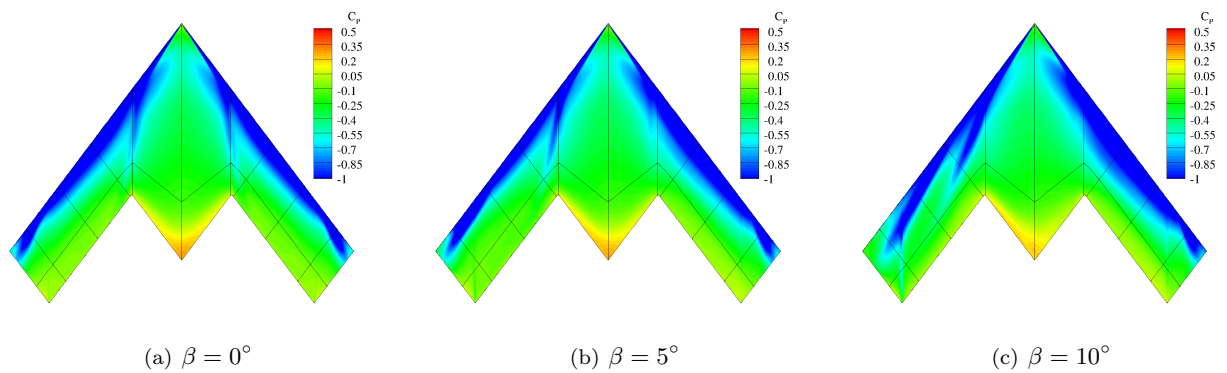


Figure 7. Run 1008 ($M=0.146$, $\alpha=15^\circ$, $Re=1.5709 \times 10^6$) surface contours.

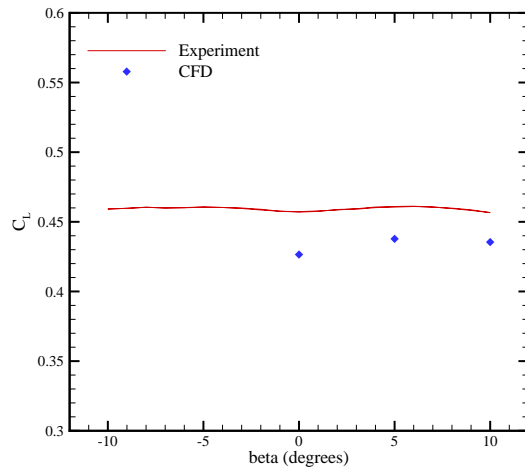
flap and the wing; secondly, using a solid wall blending region between the wing and the flap to go from the trailing edge geometry of the wing to the flap geometry in a smooth fashion. In this work the second option is used, as the first one results in extremely low quality cells in the gap due to the skewness, increases the refinement required significantly, and is detrimental to the convergence rate. Blocking the gap is also much more time consuming, and would require the generation of a new grid for each flap configuration. One of the drawbacks of the second option, however, is that the geometry is being approximated within the blending region. The effects of this will be tested in this work.

The flap geometry is known for the SACCON, so the blending process was done during the grid construction stage, instead of within the solver as is done in Ref.¹⁵ This was done by cutting the flap surface geometry, at either end, and using this as a blending region. Surfaces were then constructed within this region to obtain continuity between the wing and the flap in the spanwise direction, Fig. 5. The blocking generated for the grid in Section III.A can then be loaded onto this new geometry, and the block faces re-associated so that the original grid connectivity is maintained; thus, using this method, a family of additional grids was generated from the initial grid.

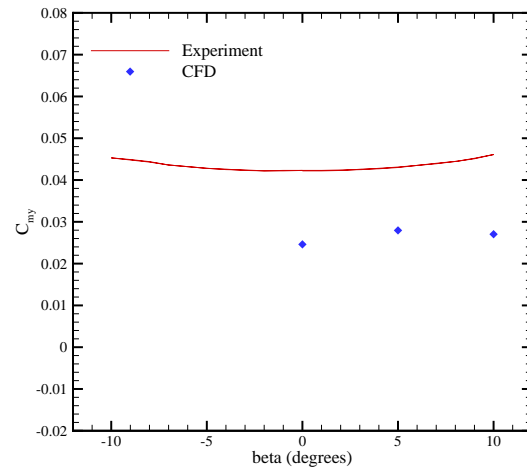
III. Low Speed Static Results

A. Results with no control surface deflections

Steady-state results at $\alpha = 10^\circ$ and 15° were simulated, with angles of sideslip $\beta = 0^\circ, 5^\circ, 10^\circ$. The lift and pitching moment coefficients, are given in Figs. 8 and 9. The underprediction of these coefficients, as in Fig. 3, can be seen; a comparison of the aerodynamic coefficients with other CFD codes used within the AVT-201 Task Group can be found in Ref.¹⁸ The surface pressure contours for these cases are given in Figs. 6 and 7; the apex and tip vortices are visible for the cases at $\alpha = 15^\circ$.

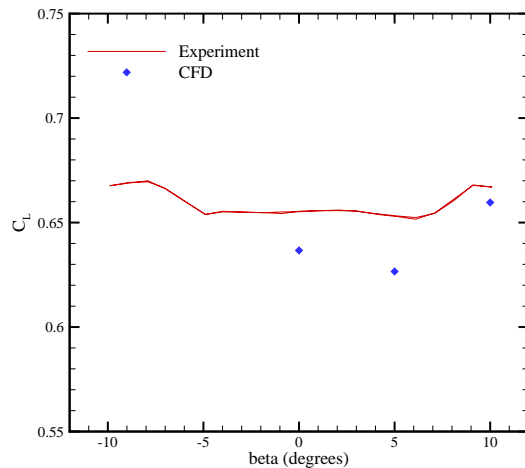


(a) Lift coefficient

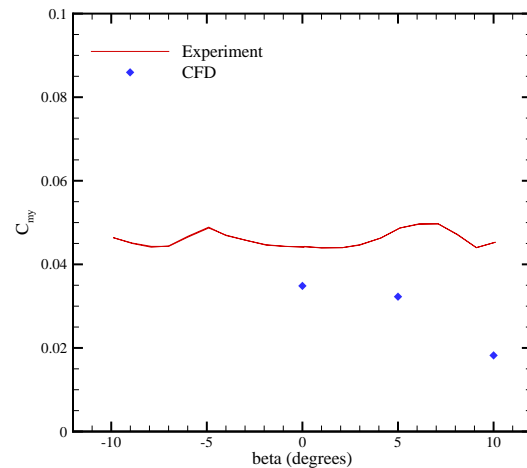


(b) Pitching moment coefficient

Figure 8. Integral data comparing experimental data and CFD for Run 1007 ($M=0.146$, $\alpha=10^\circ$, $Re=1.5709 \times 10^6$).



(a) Lift coefficient



(b) Pitching moment coefficient

Figure 9. Integral data comparing experimental data and CFD for Run 1008 ($M=0.146$, $\alpha=15^\circ$, $Re=1.5709 \times 10^6$).

The pressure coefficient along various slices of the body, at the locations as seen in Fig. 1(b), are given in Figs. 10 and 11, for the cases at $\alpha = 10^\circ$ and 15° , respectively. These plots show good agreement with the experimental data at $\alpha = 10^\circ$; though small differences appear in the results with sideslip. At higher angle of attack the rounded leading edge causes the greater suction peaks, and the creation of the vortex causes discrepancies in the surface pressure coefficient plots to be more visible at $\alpha = 15^\circ$. The apex vortex is predicted, but is further inboard than in the experiment; this feature is also seen in Ref.³ It is difficult for the CFD to accurately predict the vortex size, location and strength. There are vortex substructures in the shear layer, which RANS calculations are generally not be able to resolve.¹⁷ There is also difficulty in predicting the separation along the rounded leading edge, which occurs at this higher angle of attack range; and the separation line is especially sensitive to the turbulence model used.^{16,17} As these are steady state calculations, then the unsteady flow phenomena associated with leading edge vortices are not predicted.

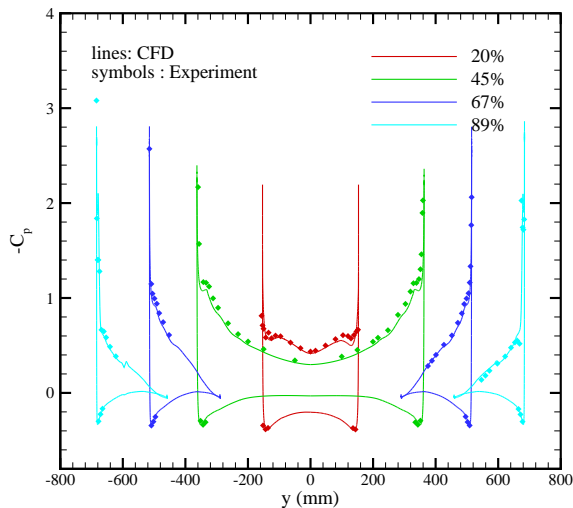
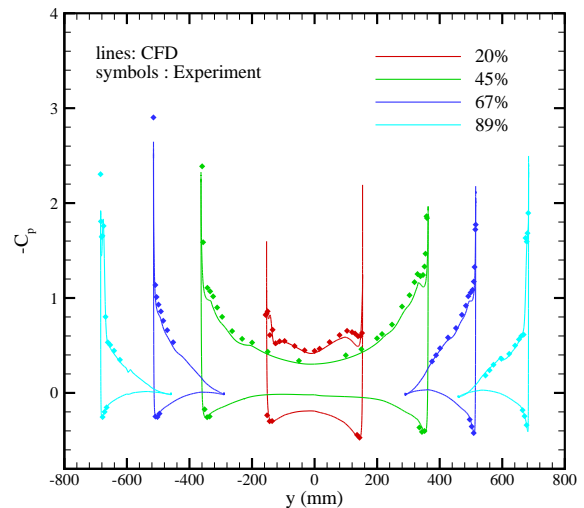
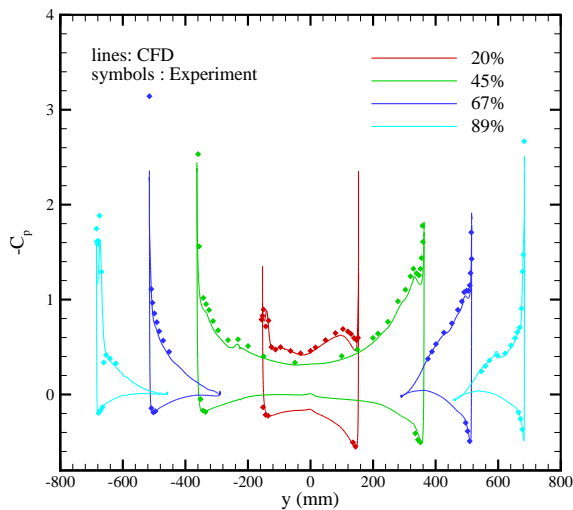
(a) $\beta = 0^\circ$ (b) $\beta = 5^\circ$ (c) $\beta = 10^\circ$

Figure 10. Run 1007 ($M=0.146$, $\alpha=10^\circ$, $Re=1.5709 \times 10^6$) pressure coefficients comparing experimental data and results from PMB.

B. Results with control surface deflections

Control surface deflections are modelled by a mesh deformation, as described in Section II.C; and a test was first made to determine the effect of the width of the blending used. For this, three geometries were used for the left outboard $+20^\circ$, left inboard $+20^\circ$ configuration: this is not one of the cases in the test matrix, and is only performed to test the blending. The blendings across the deformation are so that they are of length 15% (narrow), 25% (medium) and 35% (wide) of the flap chord. The pressure coefficient at various slices along the wing and the convergence histories are given in Figs. 12 and 13, at angles of attack 10° and 15° , respectively. From these plots we can determine that there is no difference between the blending gradients in the solutions (though none of the slices coincide with the blending region itself); and the difference in convergence rates is negligible. It should be noted, however, that the narrow blending can sometimes cause problems with the grid quality when it is loaded over the geometry. A steeper slope for the blending can stretch and twist the blocks over this region so that negative volumes occur in the far-field. To balance this problem with the problem of over simplifying the geometry, which occurs with the wide blending, the medium blending of 25% of the flap chord is used for the remainder of calculations in this work.

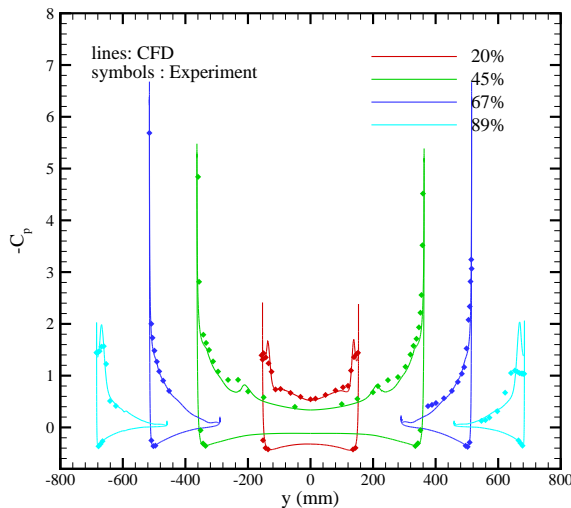
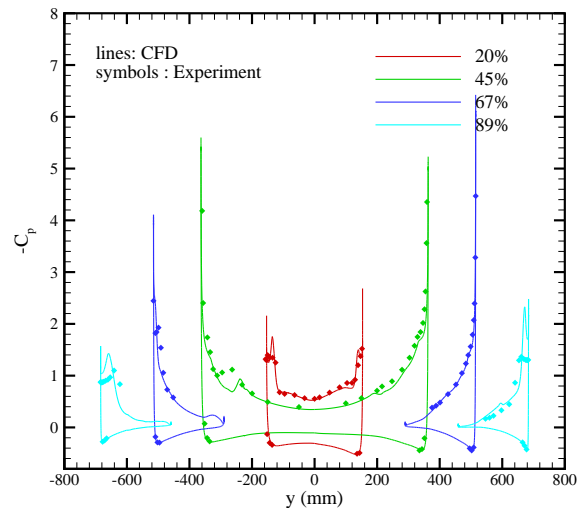
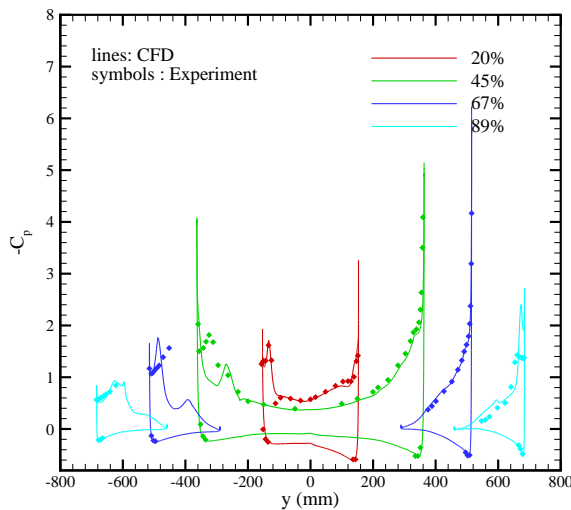
(a) $\beta = 0^\circ$ (b) $\beta = 5^\circ$ (c) $\beta = 10^\circ$

Figure 11. Run 1008 ($M=0.146$, $\alpha=15^\circ$, $Re=1.5709 \times 10^6$) pressure coefficients comparing experimental data and results from PMB.

The low speed, static calculations from the AVT-201 Task Group common test matrix, summarised in Table 1, were performed at $M = 0.146$, $Re = 1.5709 \times 10^6$, at angles of attack 10° and 15° . The pitching and rolling moment coefficients are presented in Figs. 14(a) and 14(b), respectively. The results along the roll axis are good, but there is the same offset from the pitching moment data as in Figs. 8 and 9. For clarity, the values when control surfaces have not been deployed have been subtracted in Figs. 14(c) and 14(d), for the pitch and rolling coefficients respectively. The roll coefficient is very small with no control surface deflections at $\beta = 0^\circ$, so the difference between Figs. 14(b) and 14(d) is also very small. The method of control surface modelling follows the same behaviour as the experiment for the pitching moment coefficient, though it slightly underpredicts the absolute change in the coefficient value.

The pressure coefficient at various locations along the wing are given, with the experimental data, for each of the common test matrix cases at $\alpha = 10^\circ$ and $\alpha = 15^\circ$ in Figs. 15 and 16, respectively. The results agree reasonably well with the experimental data; and the effect of the control surfaces is very small. The results at the higher angle of attack do not agree as well with the experimental data as those at the lower angle of attack; though, generally, this is in the same locations as for the cases with no control surface deflections in Section III.A. Of the control surfaces, it appears that the outboard -20° deflection (when the flow has to pass up, over the surface) deviates most from the experiment.

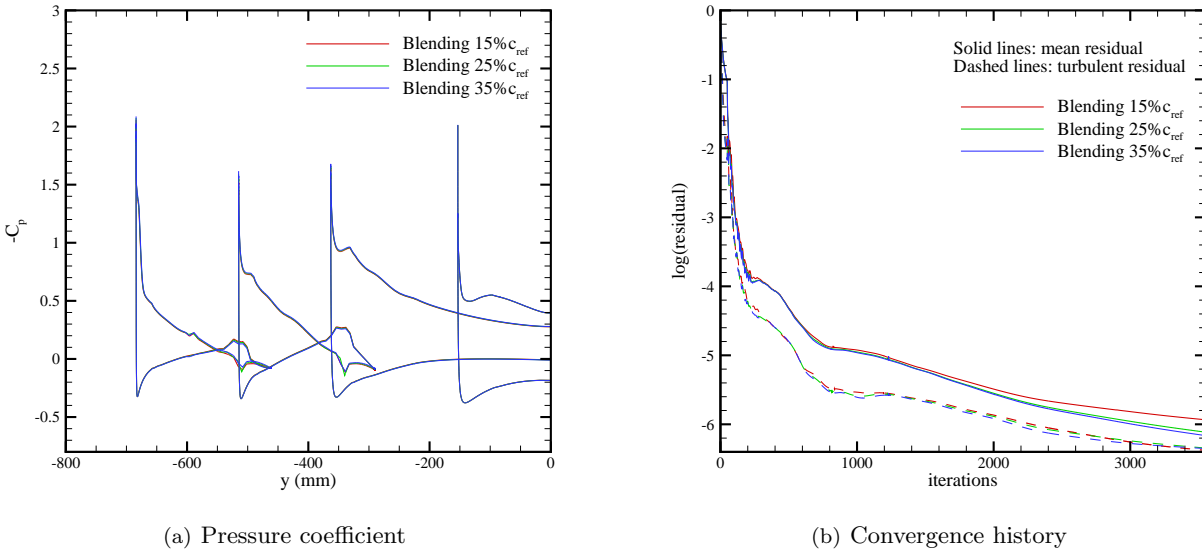


Figure 12. Comparison of results using blendings of different gradients for LOB +20 LIB +20 configuration at $M=0.146$, $\alpha=10^\circ$, $Re=1.5709 \times 10^6$.

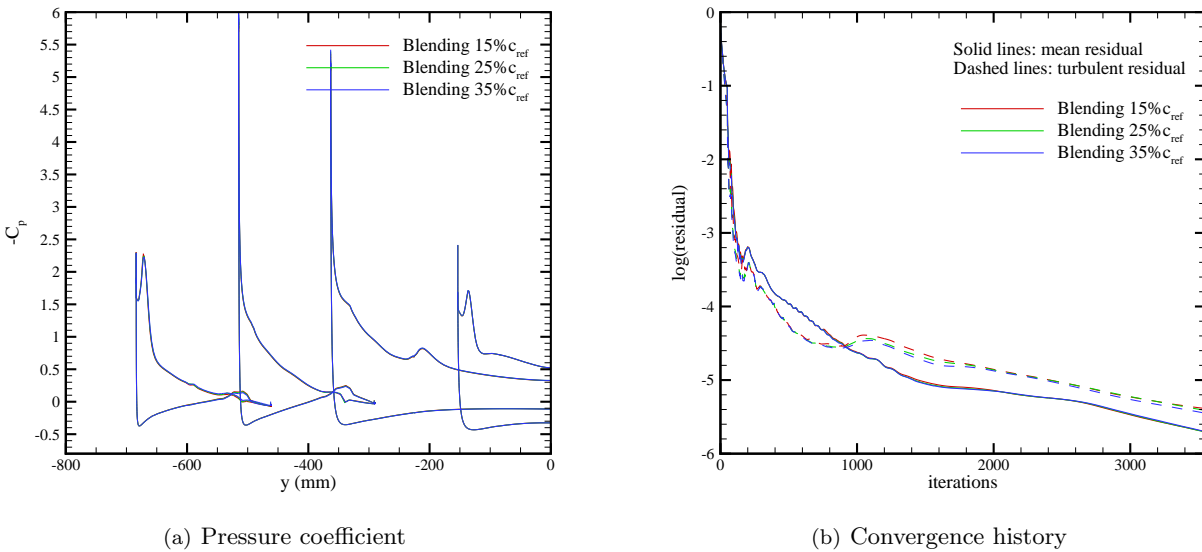


Figure 13. Comparison of results using blendings of different gradients for LOB +20 LIB +20 configuration at $M=0.146$, $\alpha=15^\circ$, $Re=1.5709 \times 10^6$.

IV. High Speed Static Results

A. Results with no control surface deflections

The high speed test cases in this work are at mean freestream conditions $M=0.7$ and $Re=18.81$ million. This effectively lowers the angle of attack range in which the tip vortex is formed; hence, the results are simulated at $\alpha = 5^\circ$ and 10° . The pressure coefficient contours along the surface are given in Figs. 17(a) and 17(b) for these respective angles. These plots show that there is some spanwise flow near the trailing edge at low angle of attack; and the flow has separated at the trailing edge at the higher angle.

Unfortunately there were no pressure measurements made in the high speed experiments, so comparisons are limited to the forces and moments: the lift, drag and pitching moment coefficients are given in Fig. 18. The plots show that these characteristics are reasonably well predicted; and the pitching moment coefficient agrees more with the free transition experimental data.

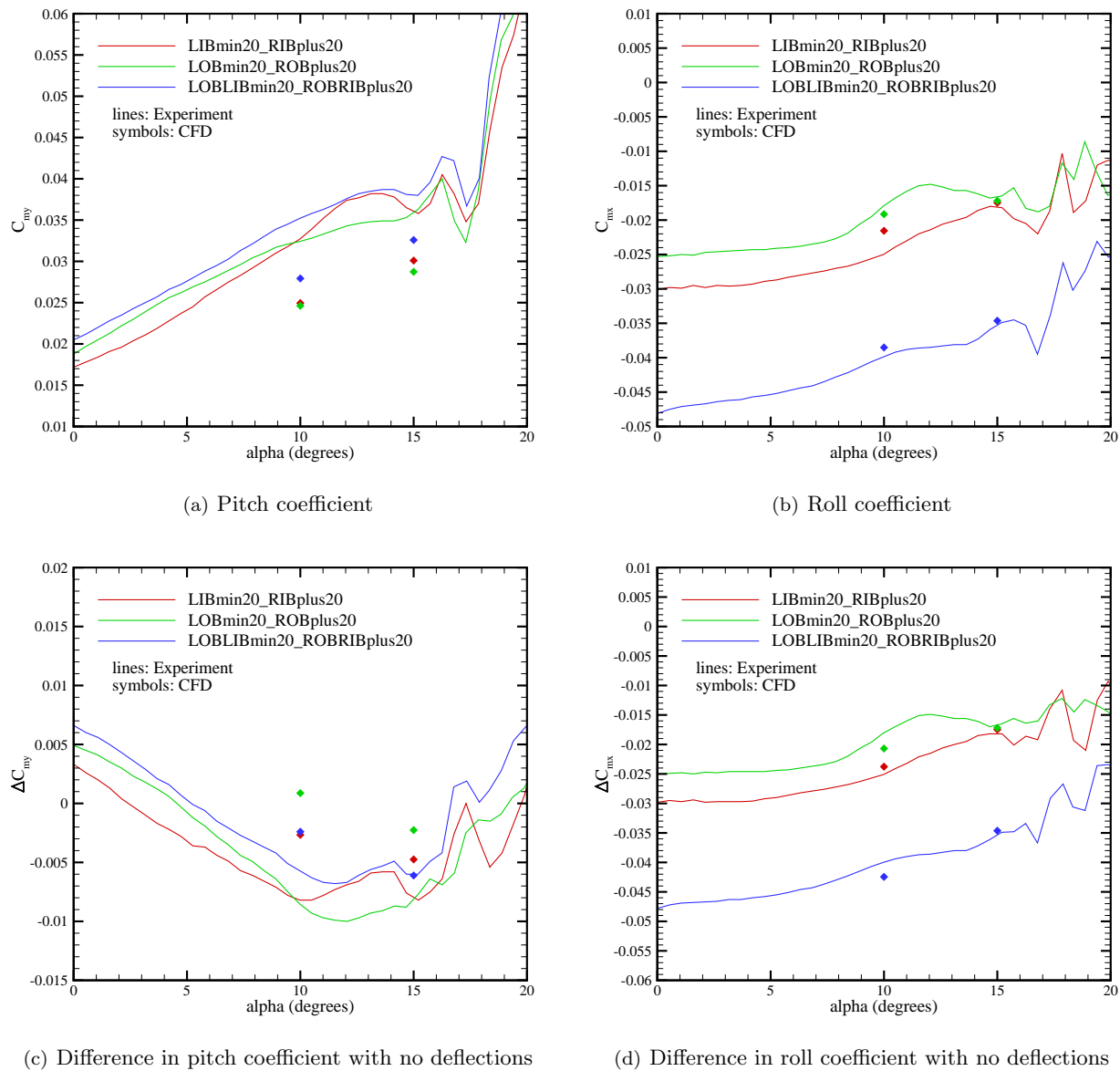
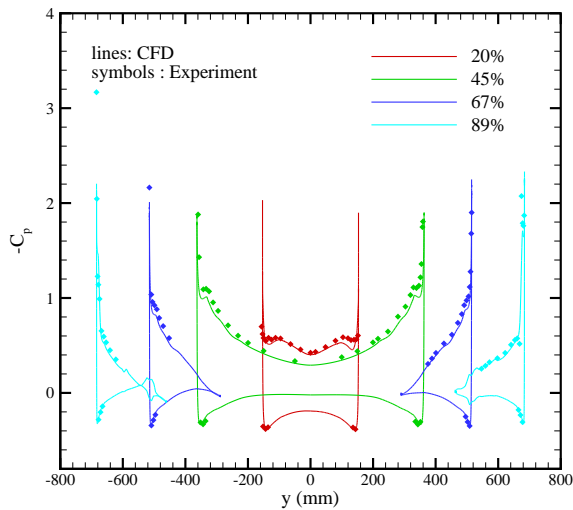


Figure 14. Integral data comparing experimental data and CFD for control surface deflections in the common test matrix at $M=0.146$, $Re=1.5709 \times 10^6$.

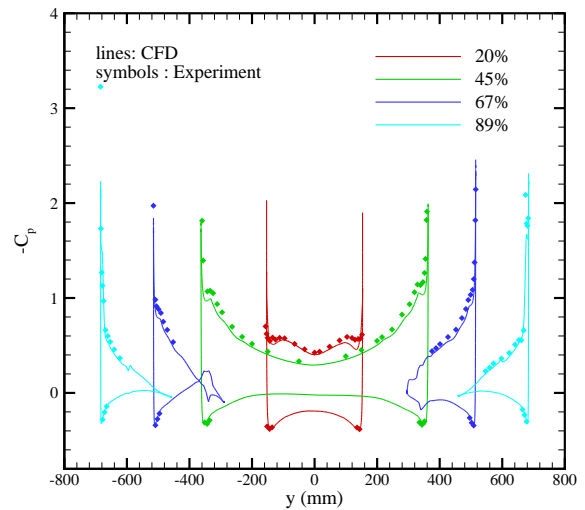
B. Results with control surface deflections

Four additional cases, with individual control surface deflections, as summarised in Table 1, were also performed. The grids were created in the same way as for the low speed grids, as described in Section II.C.

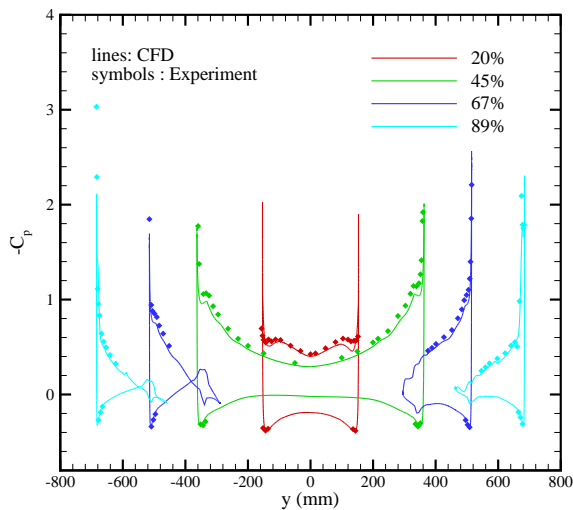
The difference in pitching and rolling coefficients, between the cases with control surface deflections and the results with no deflections, are given in Fig. 19. The offsets for pitching moment are reasonably well predicted; the largest disagreement is at the lower angle of attack $\alpha = 5^\circ$. This is possibly because the flow is in the angle of attack region in which the spanwise flow is starting to separate along the control surfaces; the CFD may be struggling to predict this location exactly. By the time the angle of attack has increased to $\alpha = 10^\circ$ the flow has already separated. The trailing edge controls are unlikely to be effective or well behaved in this separated region.



(a) LOB -20, ROB +20



(b) LIB -20, RIB +20



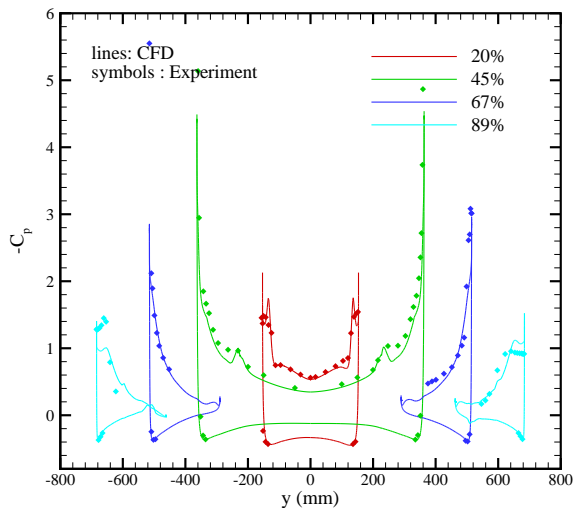
(c) LOBLIB -20, ROBRIB +20

Figure 15. Pressure coefficient plots for control surface deflections at $M=0.146$, $\alpha=10^\circ$, $Re=1.5709 \times 10^6$.

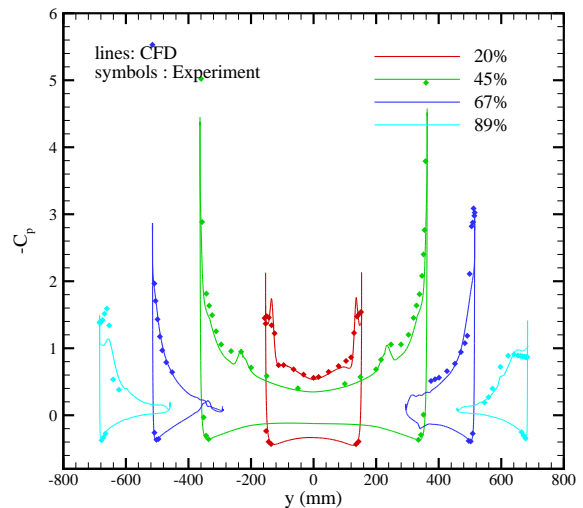
V. Forced Oscillatory Motion Results

Forced oscillatory motion cases are presented for pitching and yawing motions. For each motion type there is a case at a nominal pitch angle in which the flow field is relatively benign, and one at a higher angle, when the flow is more non-linear: these angles are at $\Theta_0 = 10^\circ$ and $\Theta_0 = 15^\circ$. The effect of the time-step is analysed in a study: the cases have 128, 256 and 512 steps per cycle, and, if needed, the number of steps is further increased to 1024 per cycle. The simulations include dynamic pitch oscillations at $\Theta_0 = 10^\circ$, $\Delta\Theta = 4.7^\circ$, which can be seen in Fig. 20, and $\Theta_0 = 15^\circ$, $\Delta\Theta = 4.7^\circ$, which can be seen in Fig. 21. The lift and moment coefficients for the experiment and CFD, with the nominal start point steady values subtracted, are presented with respect to the angle of motion. The rolling and yawing moments for dynamic yaw oscillation at $\Theta_0 = 10^\circ$, $\Delta\Psi = 5.0^\circ$ are presented in Fig. 23, and $\Theta_0 = 15^\circ$, $\Delta\Psi = 5.0^\circ$, in Fig. 24.

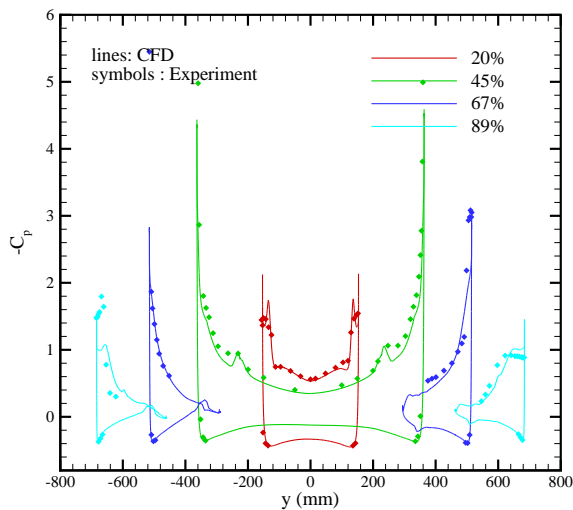
For the pitching motion at $\Theta_0 = 10^\circ$, in Fig. 20, the hysteresis in the lift coefficient loops is noticeably small. This indicates that the flow field adapts instantaneously to changes in model attitude. The lift plot shows that even though the static values have been removed from the CFD and experimental data, there is still an offset between the two. As for the static cases, this is still probably due to the sting not being modelled in these simulations. For the moment coefficient, the forced motion loops differ from the static values; the mean value at the nominal angle is lower than the static value. The mean slope of the moment



(a) LOB -20, ROB +20



(b) LIB -20, RIB +20



(c) LOBLIB -20, ROBRIB +20

Figure 16. Pressure coefficient plots for control surface deflections at $M=0.146$, $\alpha=15^\circ$, $Re=1.5709 \times 10^6$.

loops is shallower, and the hysteresis of the loop is less for the CFD than those for the experimental data for pitch angle less than 11° . Above this angle the slope for the experiment plateaus and the gradient becomes negative; the CFD does not predict this, and, in fact, the gradient actually increases slightly.

For the pitching motion at $\Theta_0 = 15^\circ$, in Fig. 21, the hysteresis for the force coefficient is very large at the highest instantaneous angles. The CFD also predicts a hysteresis; however, there is still the offset compared with the experiment, even when the static values are subtracted. There is a much greater difference between the shape of the moment coefficient loops for this nominal pitch angle. Convergence is difficult to achieve, with over a thousand time steps being required to even approach convergence. The range of pitch angle converged includes the highly non-linear regions in steady simulations, where the moment dip occurs and vortex breakdown begins.³ The loops predicted by the CFD cross at various points during the cycle, which does not happen in the experiment. The peaks and troughs do not match the experiment either: the dip on the upstroke at 18° for the experiment is not predicted at all; and where the experiment shows a peak on the downstroke at about 18° , the CFD, conversely, predicts a trough.

Due to the non-linearities in this test case, and the inability of the CFD to predict them, it is worth looking at the results at various time steps during the 1024 step cycle in more detail. Figure 22 shows the pressure coefficient contours over the SACCON surface at twelve locations during the cycle. If we begin the analysis near the nominal angle on the downstroke, Figs. 22(a) and 22(b) show that the surface contours,

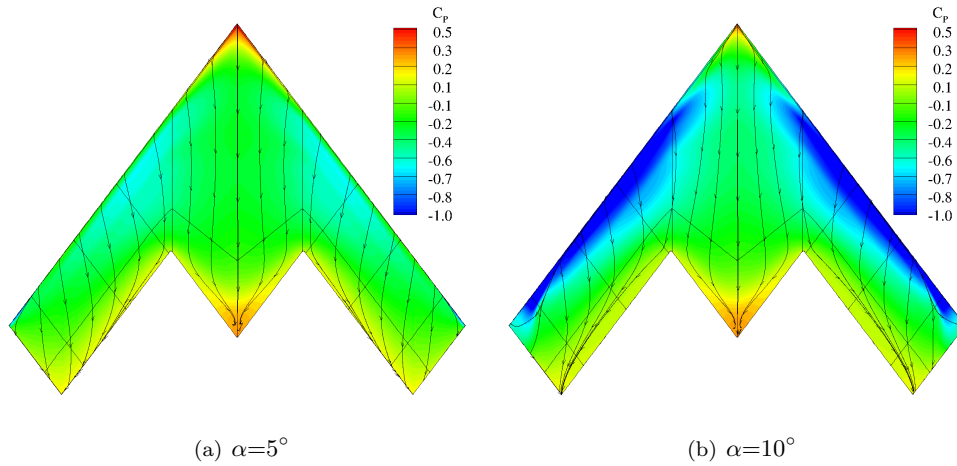
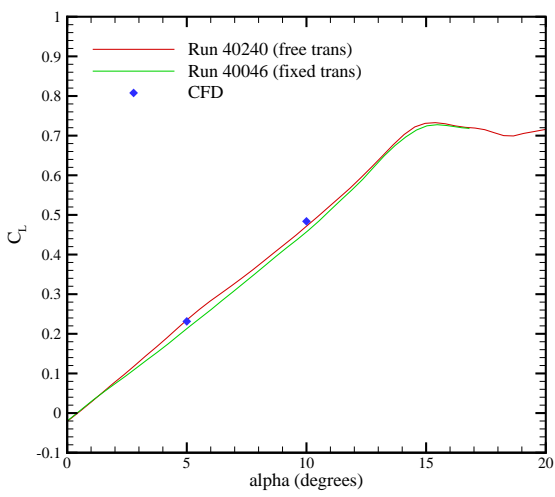
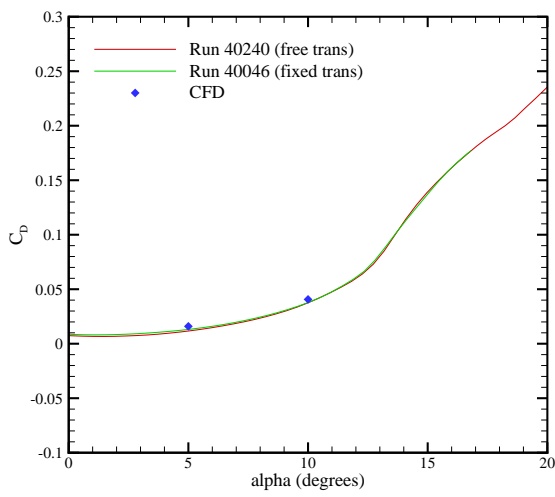


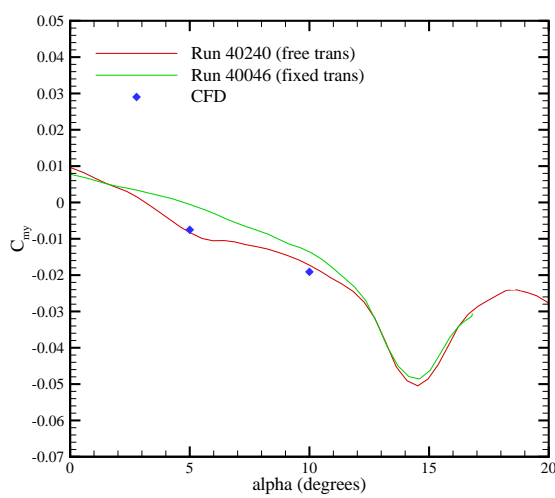
Figure 17. Run 40046 ($M=0.7$, $Re=18.81 \times 10^6$) surface contours.



(a) Lift coefficient



(b) Drag coefficient



(c) Pitching moment coefficient

Figure 18. Integral data comparing CFD with experiment for high speed tests at $M=0.7$, $Re=18.81 \times 10^6$.

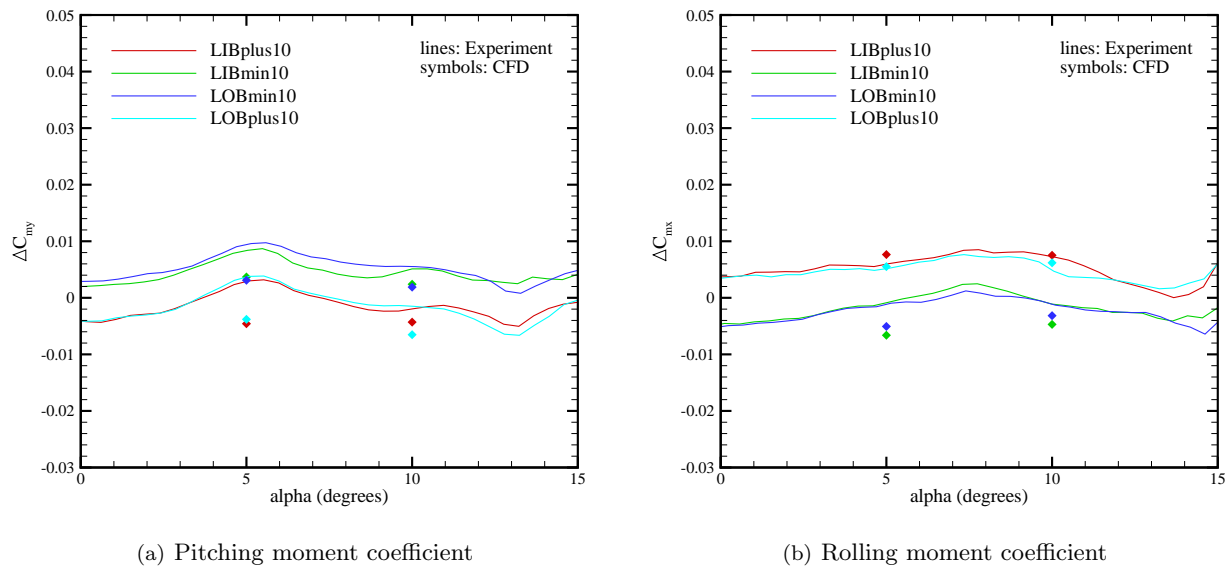


Figure 19. Integral data comparing high speed experimental data and CFD for control surface deflections in the common test matrix at $M=0.7$, $Re=18.81 \times 10^6$.

at $\Theta = 12.98^\circ$ and $\Theta = 10.57^\circ$ respectively, are very similar to the static results at this range shown in Figs. 6 and 7. The tip vortex is very small at $\Theta = 10.57^\circ$, but increases in size when the upstroke begins at $\Theta = 15.88^\circ$ in Fig. 22(c). Even though the angle has increased by 3° to $\Theta = 18.88^\circ$ in Fig. 22(d), the tip vortex has not moved a great deal. Although the vortex appears to be increasing in strength, it is not enough to offset the suction caused by the apex vortex, and the coefficient stays relatively constant in the CFD. This is in contrast with the experiment, in which a dip, similar to that in the static pitching moment plots,³ can be seen. The unsteadiness in the CFD has effectively increased the angle at which the vortex is frozen before a dip should commence; however, as the upstroke continues to $\Theta = 19.34^\circ$ and $\Theta = 19.65^\circ$, in Figs. 22(e) and 22(f) respectively, the dip still does not take place. The tip vortex has started to move inboard over the rounded leading edge, but, despite the high pitch angle, there is still some attached flow and the vortices have not merged; this is in contrast with the static results at this angle of attack.¹³ Figures 22(g) and 22(h) show, as the downstroke begins, that the flow has separated along the leading edge, and the vortices have merged, producing lots of suction behind the moment reference point; this causes a pitch down motion, which is not seen in the experiment but can be seen in Fig. 21. In Fig. 22(i) the pitch down rate slows down as the vortices begin to split; and, at $\Theta = 18.46^\circ$ on the downstroke, the coefficient increases again. If we compare the surface contours of the downstroke, Fig. 22(j), with those, at a similar angle, on the upstroke, in Fig. 22(d), we can see that the tip vortex is much stronger and further inboard. It appears that the vortices are not moving to the outboard locations on the downstroke quickly enough; and the tip vortex has still not reached the leading edge by $\Theta = 18.06^\circ$, in Fig. 22(k). Finally, at about $\Theta = 16.87^\circ$ the coefficient begins to plateau, and the surface looks similar to the static surface contours again.

Similar to the pitching motion case at $\Theta_0 = 10^\circ$, the yawing motion at $\Theta_0 = 10^\circ$ shows very little hysteresis, as can be seen in Fig. 23. The roll coefficient values are well predicted near the nominal yawing angle, though at the extremities there are some differences due to a slightly steeper loop than in the experiment. The yaw coefficient loops are also well predicted: the shape of the loop is similar, and the offset of the values between the experiment and CFD at corresponding yaw angles is very small.

The roll coefficient for the yaw oscillation at $\Theta_0 = 15^\circ$ is more non-linear than at $\Theta_0 = 10^\circ$, as can be seen in Fig. 24. Within the range $\Psi = \pm 1.5^\circ$ the flow is relatively linear; however, outside this range the mean gradient of the loops in the experiment plateau, and the hysteresis increases slightly. The CFD predicts the roll coefficient well within $\Psi = \pm 1.5^\circ$, but the non-linearities outside these angles are not predicted at all. The non-linearities in the yaw coefficient are not predicted either; and, as with the yawing motion at $\Theta_0 = 10^\circ$, there is an offset, with the values of the CFD being underpredicted.

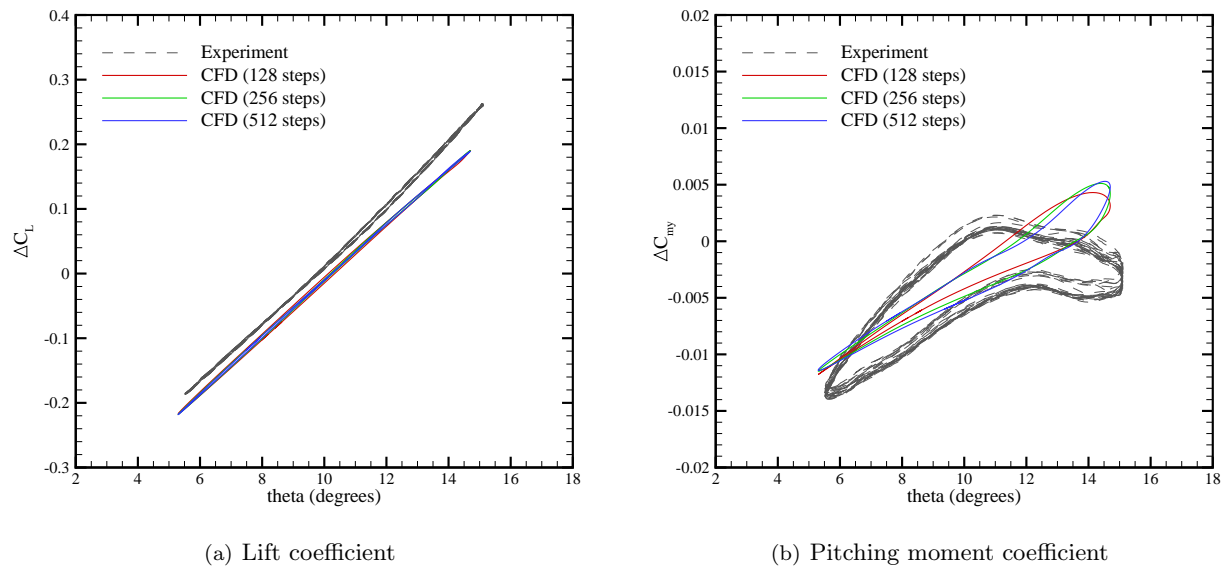


Figure 20. Lift and moment coefficients for pitching motion ($\Theta_0=10^\circ$, $\Delta\Theta=4.7^\circ$, $f=1\text{Hz}$) comparing experimental data and results from PMB at $M=0.146$, $\text{Re}=1.5709\times 10^6$.

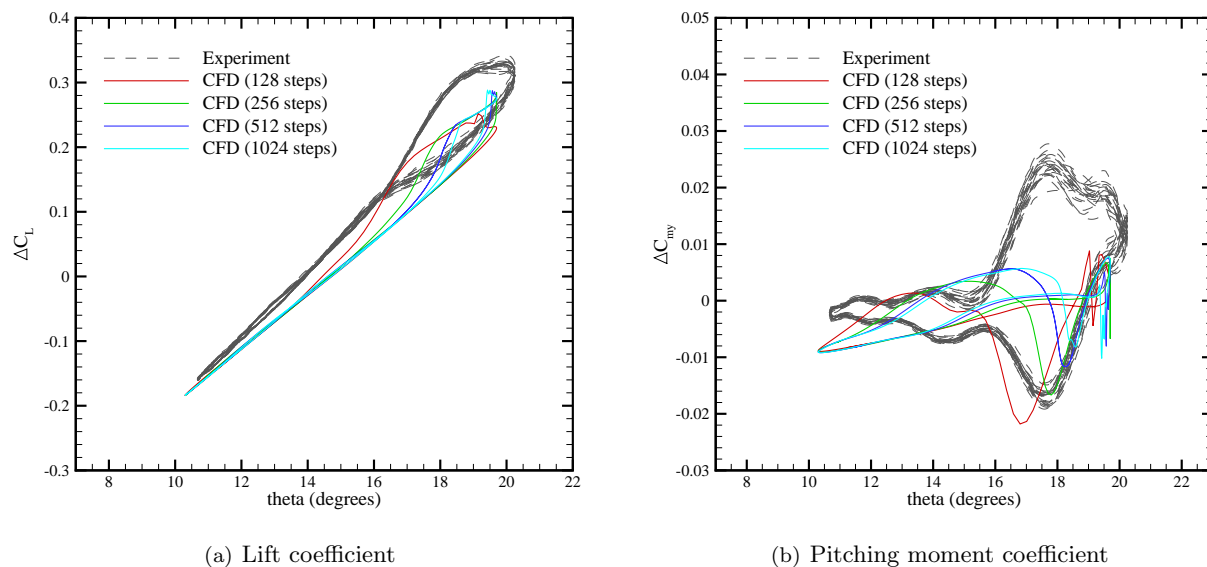


Figure 21. Lift and moment coefficients for pitching motion ($\Theta_0=15^\circ$, $\Delta\Theta=4.7^\circ$, $f=1\text{Hz}$) comparing experimental data and results from PMB at $M=0.146$, $\text{Re}=1.5709\times 10^6$.

VI. Conclusions

This work evaluates the ability of CFD techniques to predict the flow, at low and high speed, over a generic UCAV, both with and without control surfaces deflected. This flow is complex due to the vortices that develop, both in strength and location, and the separation that occurs along the leading edge of varying thickness. The solver used to simulate this flow is a well validated, cell-centred, block-structured code; and it solved the RANS equations, with a two-equation turbulence model.

Apart from the well-documented underprediction of the lift and moment coefficients, the results show that the method is sufficient for the low angle of attack range. At the higher angle of attack the tip vortex has formed and begins to move across the surface as the angle increases. The pressure coefficient plots show that the vortices, although predicted, are not at the correct strength or location. As the vortical flow features

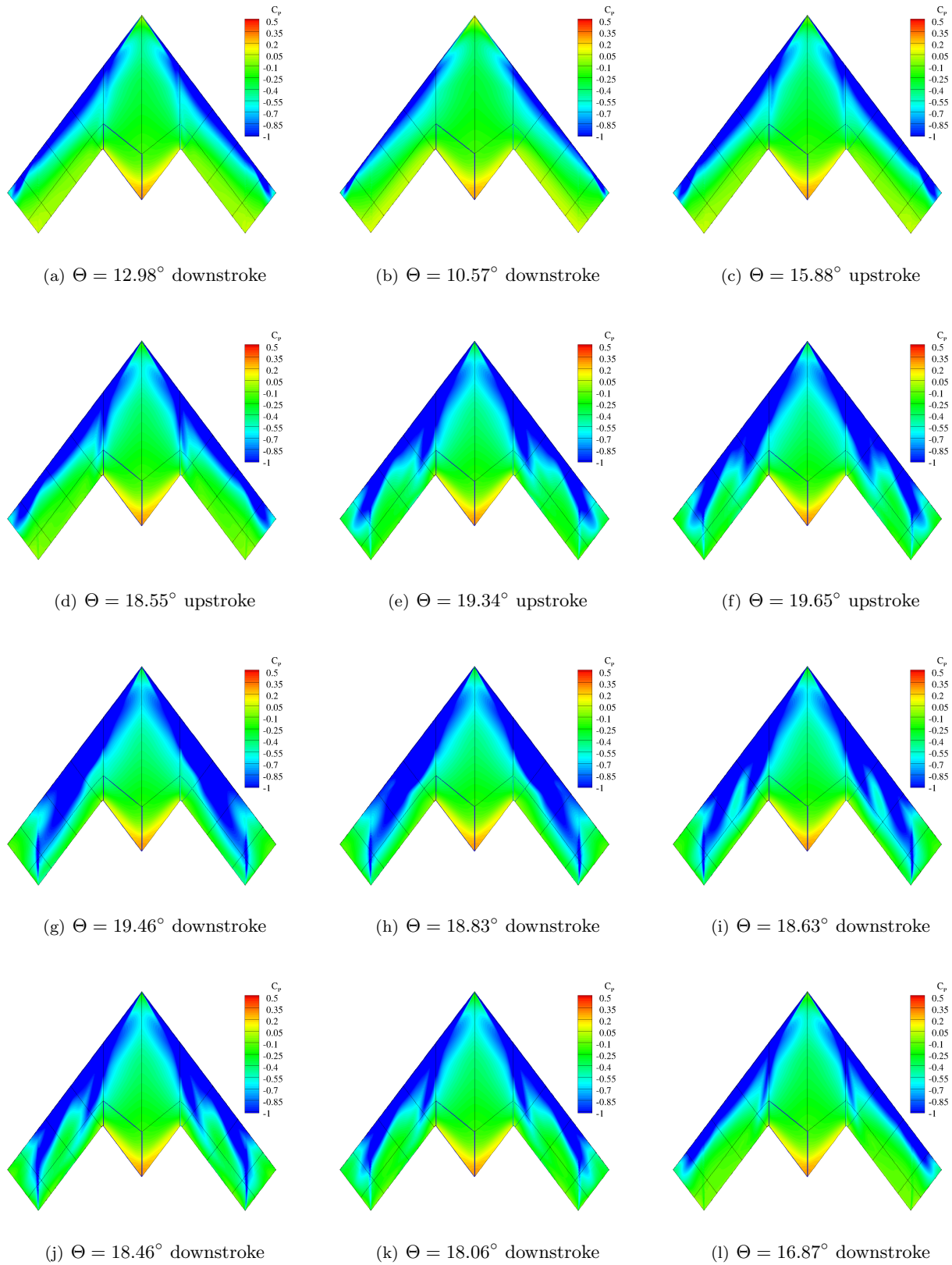


Figure 22. Surface contours at various times during pitching motion ($\Theta_0=15^\circ$, $\Delta\Theta=4.7^\circ$, $f=1\text{Hz}$) at $M=0.146$, $\text{Re}=1.5709 \times 10^6$.

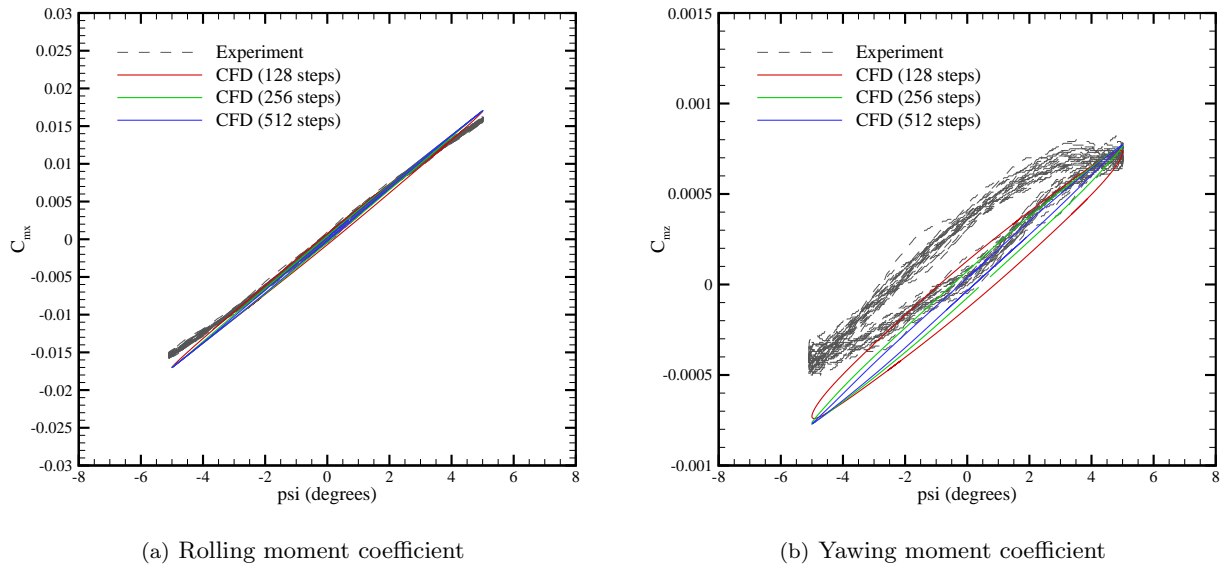


Figure 23. Rolling and yawing coefficients for yawing motion ($\Theta_0=10^\circ$, $\Delta\Psi=5.0^\circ$, $f=1\text{Hz}$) comparing experimental data and results from PMB at $M=0.146$, $\text{Re}=1.5709\times 10^6$.

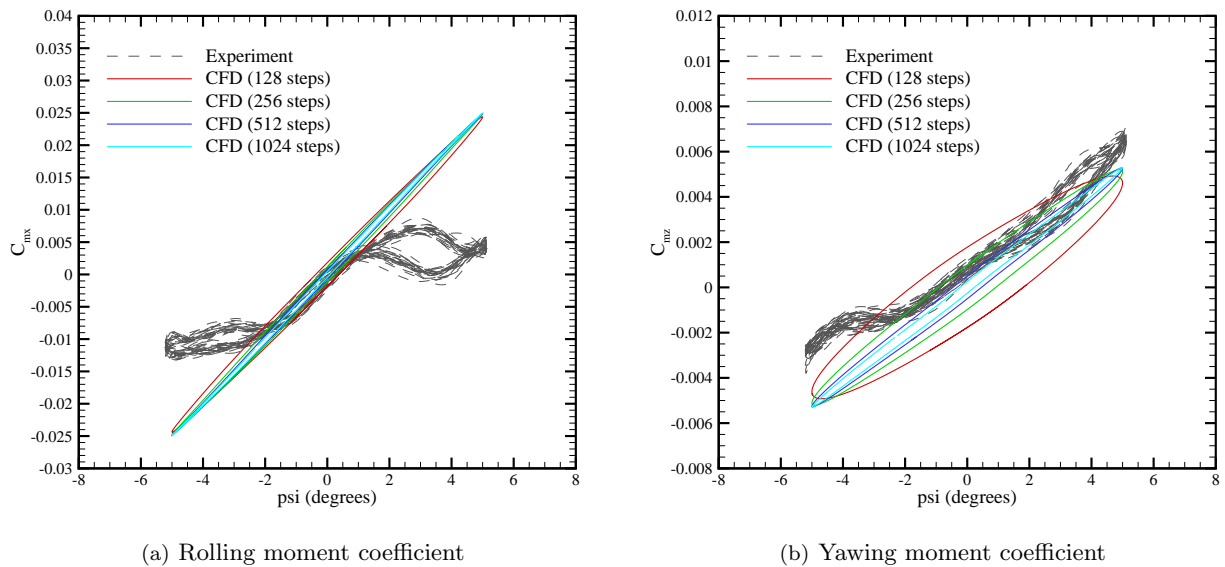


Figure 24. Rolling and yawing coefficients for yawing motion ($\Theta_0=15^\circ$, $\Delta\Psi=5.0^\circ$, $f=1\text{Hz}$) comparing experimental data and results from PMB at $M=0.146$, $\text{Re}=1.5709\times 10^6$.

are typically unsteady, then steady state calculations are not fully accurate. For these reasons future work will look at improving the cases at the higher angle of attack using detached-eddy simulation.

The addition of the control surfaces has not caused any serious difficulties in generation or the results. The pressure coefficient plots are good when compared with experiment: the major differences also appear in the case with no control surface deflections. The largest deviation from experiment resulting from the control surfaces being deployed appears to be for the outboard -20° deflection when the flow has to pass up and over the surface. The offsets for the moment coefficients, for both low and high speeds, are predicted, with the roll coefficients being particularly well predicted.

The unsteady results in this work are at nominal pitch angles 10° and 15° ; as a result, they simulate the cases before and after the tip vortex of the SACCON is formed. The unsteady, pitching oscillation

simulations, therefore, move in and out of this flow field range. The difference between the experimental and CFD pitching moment coefficients appear, again, to be as a result of incorrect vortex prediction. The location that the flow separates fully, and tip and apex vortex merge, is very important; but it is clear that solving the RANS equations with a turbulence model is unable to accurately determine this. The cases at angle $\Theta_0 = 15^\circ$, for both pitch and yaw motions, deviate most from the experimental data; they also display the most unsteady flow characteristics, as they need more time steps for the solution to approach convergence. As a result, at least these two cases will also be run using detached-eddy simulation to see if there is any improvement.

Acknowledgments

This research has been supported by BAE SYSTEMS and the Technology Strategy Board as part of the Simulation at Off-Design Conditions (SimOD) group. Special thanks is also extended to the AVT-201 team members for their efforts in obtaining CFD and experimental data, and also for their subsequent discussions and advice.

References

- ¹Loeser, T. D., Vicroy, D. D., and Schüette, A., "SACCON Static Wind Tunnel Tests at DNW-NWB and 14x22 NASA LaRC," 28th AIAA Applied Aerodynamics Conference, 2010, Chicago, Illinois.
- ²NATO RTO AVT-161 Final Report, 2011.
- ³Schüette, A., Hummel, D., and Hitzel, S. M., "Numerical and experimental analyses of the vortical flow around the SACCON configuration," 28th AIAA Applied Aerodynamics Conference, 2010, Chicago, Illinois.
- ⁴Cummings, R. M., and Schütte, A., Integrated Computational/Experimental Approach to Unmanned Combat Air Vehicle Stability and Control Estimation. *Journal of Aircraft*, Vol. 49, No. 6 (2012), pp. 1542-1557.
- ⁵Cummings, R. M., and Schüette, A., "The NATO STO Task Group AVT-201 on 'Extended Assessment of Stability and Control Prediction Methods for NATO Air Vehicles'," 32nd AIAA Applied Aerodynamics Conference, AIAA, Reston, Virginia (submitted for publication).
- ⁶Huber, K. C., Vicroy, D. D., Schüette, A., and Huebner, A., "UCAV model design and static experimental investigations to estimate control device effectiveness and S&C capabilities," 32nd AIAA Applied Aerodynamics Conference, AIAA, Reston, Virginia (submitted for publication).
- ⁷Vicroy, D. D., Huber, K. C., Loeser, T. D., and Rohlf, D., "Low-speed Dynamic Wind Tunnel Test Analysis of a Generic 53° Swept UCAV Configuration" 32nd AIAA Applied Aerodynamics Conference, AIAA, Reston, Virginia (submitted for publication).
- ⁸Rein, M., Irving, J., Rigby, G., and Birch, T. J., "High speed static experimental investigations to estimate control device effectiveness and S&C capabilities," 32nd AIAA Applied Aerodynamics Conference, AIAA, Reston, Virginia (submitted for publication).
- ⁹Kennett, D. J., "SimOD Report: Work Package 2," University of Liverpool internal report TN14-001, 2014.
- ¹⁰Badcock, K. J., Richards, B. E., and Woodgate, M. A., "Elements of computational fluid dynamics on block structured grids using implicit solvers," *Progress in Aerospace Sciences* 36 (2000) pp 351-392.
- ¹¹Brandsma, F. J., Kok, J. C., Dol, H. S., and Elsenaar, A., "Leading edge vortex flow computations and comparison with DNW-HST wind tunnel data," *Proceedings of the NATO RTO/AVT Symposium on Vortex Flows and High Angle of Attack*, NATO RTO/AVT, 2001.
- ¹²Jameson, A., "Time Dependent Calculations Using Multigrid, with Applications to Unsteady Flows Past Airfoils and Wings," AIAA Paper 91-1596, AIAA 10th Computational Fluid Dynamics Conference (1991) Honolulu, Hawaii.
- ¹³Vallespin, D., Da Ronch, A., Badcock, K. J., and Boelens, O., "Validation of Vortical Flow Predictions for a UCAV Wind Tunnel Model," 28th AIAA Applied Aerodynamics Conference, 2010, Chicago, Illinois.
- ¹⁴Vallespin, D., "Development of a Process and Toolset to Study UCAV Flight Mechanics using Computational Fluid Dynamics," Ph.D. Thesis, University of Liverpool.
- ¹⁵Rampurawala A. M., "Aeroelastic analysis of aircraft with control surfaces using CFD," Ph.D. Thesis, University of Glasgow, Glasgow, UK.
- ¹⁶Cummings, R. M., Jirasek, A., Petterson, K., and Schmidt, S., "SACCON Static and Dynamic Motion Flow Physics Simulation Using Cobalt," 28th AIAA Applied Aerodynamics Conference, 2010, Chicago, Illinois.
- ¹⁷Tormalm, M., and Schmidt, S., "Computational study of static and dynamic vortical flow over the delta wing SACCON configuration using the FOI flow solver Edge," 28th AIAA Applied Aerodynamics Conference, 2010, Chicago, Illinois
- ¹⁸Jirásek, A., Cummings, R. M., Schüette, A., and Huber, K., "The NATO STO AVT-201 Task Group on Extended assessment of Stability and Control Prediction Methods for NATO Air Vehicles: Summary, Conclusions and Lessons Learnt" 32nd AIAA Applied Aerodynamics Conference, AIAA, Reston, Virginia (submitted for publication).